Supporting Information: Understanding the Effect of Lead Iodide Excess on the Performance of Methylammonium Lead Iodide Perovskite Solar Cells

Zeeshan Ahmad,[†] Rebecca A. Scheidt,[‡] Matthew P. Hautzinger,[‡] Kai Zhu,[‡] Matthew C. Beard,[‡] and Giulia Galli*[,†,¶,§]

†*Pritzker School of Molecular Engineering, University of Chicago, Chicago, Illinois 60637, United States*

‡*Chemistry & Nanoscience Center, National Renewable Energy Laboratory, Golden, Colorado 80401, United States*

¶*Department of Chemistry, University of Chicago, Chicago, Illinois 60637, United States*

§*Argonne National Laboratory, Lemont, Illinois 60439, USA*

E-mail: gagalli@uchicago.edu

Computational Details

All DFT calculations have been performed using the plane wave code Quantum Espresso.[1,2] The Perdew–Burke-Ernzerhof (PBE) exchange-correlation functional[3] without spin-orbit coupling was used for geometry optimizations. On the relaxed structures, single point DFT calculations using the Heyd–Scuseria–Ernzerhof (HSE) hybrid functional[4] with spin-orbit coupling were performed. The DFT-D3 scheme proposed by Grimme was used to account for the van der Waals dispersion.[5] For PBE calculations, we used the ultrasoft GBRV pseudopotentials with the suggested energy cutoffs of 40 Ry for the wavefunction and 320 Ry for the density.[6] For the HSE calculations, we used SG15 ONCV pseudopotentials[7] with a 70 Ry energy cutoff for the wavefunction, 280 Ry for the density, and 70 Ry for the exact exchange operator. For interfacial calculations, we used I pseudopotential with 7 valence electrons instead of 17 to reduce the computational cost. The fraction of the exact exchange used for both MAPI and PbI_2 was 0.43 which has been shown to provide a better agreement with the experimental band gap of MAPI.[8] For PbI_2 as well, the band gap using this value of exact exchange is in agreement with experiment as shown in Table S1.[9] For surfaces and interfaces, the periodic images were separated by a minimum of 15 Å vacuum for PBE calculations and 10 Å for the HSE calculations to save memory. HSE calculations performed using 15 Å vacuum showed negligible change in the energies. The pymatgen[10] and atomic simulation environments[11] were used for generating surface and interfacial structures while the visualization was done using the VESTA package.[12] For defect formation energy calculations using HSE functional, reduced energy cutoffs of 40 Ry for the wavefunction and 80 Ry for the exact exchange operator were used which have been shown to agree well with those calculated at 70 Ry energy cutoffs due to error cancellation for the pristine and defective structures.[13] For MAPI, we used the experimental lattice constants 8.849 Å and 12.642 Å .[14] For PbI_2, the structure # 9009114[15] from crystallography open database[16] with spacegroup $P\bar{3}m1$ was used. The ionic positions are relaxed according to convergence criteria of at most 0.001 Ry/Bohr for forces and 0.0001 Ry for energies. For some pristine structures, reduced

Table S1: Band gaps obtained using hybrid functional with fraction of exact exchange = 0.43.

Material	Band gap (eV)
MAPI	1.42
PbI_2	2.36

force convergence criteria had to be used to obtain the defect formation energies due to the shallow nature of the energy landscape. An example of an interfacial defect is shown in Fig. S1

The interfaces identified are shown in Table S2 have in plane lattice vectors normal to each other. This enforces the PbI_2 surface to be $(1\,0\,\bar{1}\,0)$ with its lattice vectors b and c in the plane of the interface.

Table S2: Possible interfaces between different surfaces of MAPI and PbI_2. All interfaces studied use the PbI_2 termination of MAPI in order to study PbI_2 excess effects. The table shows the surface facets of MAPI and PbI_2, the in plane lattice vectors a_1 and a_2 and strains in those directions. For interfaces besides those with MAPI (0 0 1) in rows 1 and 2, we fixed the in-plane lattice vectors to the MAPI values since the existence of small amounts of PbI_2 is not expected to influence MAPI axes considerably. We group the interfaces into types 1, 2, and 3 as shown in the table. Note that this type is different from the type of band alignment for which Roman numerals I and II have been used.

Type 1: MAPI (0 0 1) with Pb terminated PbI_2 (1 0 $\bar{1}$ 0), with cell relaxation					
Lattice vector	MAPI	PbI_2	Interface	strain MAPI (%)	strain PbI_2 (%)
a_1	a=8.849	2a=9.11	9.06	2.33	-0.60
a_2	a=8.849	c=6.977	8.38	-5.33	20.07
Type 1: MAPI (0 0 1) with I terminated PbI_2 (1 0 $\bar{1}$ 0), with cell relaxation					
a_1	a=8.849	2a=9.11	9.070	2.50	-0.44
a_2	a=8.849	c=6.977	8.358	-5.54	19.80
Type 2: MAPI (1 1 0) with PbI_2 (1 0 $\bar{1}$ 0) Lattice vectors fixed to MAPI values; two Interfaces: Pb and I terminations of PbI_2					
a_1	c=12.642	3b=13.665	12.642	0	-7.49
a_2	$\sqrt{2}$a=12.514	2c=13.954	12.514	0	-10.32
Type 3: MAPI (0 0 1) rotated 45 degrees about [0 0 1] axis with PbI_2 (1 0 $\bar{1}$ 0) Lattice vectors fixed to MAPI values; two Interfaces: Pb and I terminations of PbI_2					
a_1	$\sqrt{2}$b=12.514	3b=13.665	12.514	0	-8.42
a_2	$\sqrt{2}$a=12.514	2c=13.954	12.514	0	-10.32

The local VBM and CBM energy levels are estimated using the local density of states $D(E,z)$ and the Fermi level E_F as:[17,18]

$$\int_{VBM}^{E_F} D(E,z)dE = \int_{E_F}^{CBM} D(E,z)dE = \Delta \int_{-\infty}^{E_F} D(E,z)dE \quad (1)$$

where Δ was set to 0.001 for the interfaces. A macroscopic average of the integrals over 6 Å (typical Pb-Pb distance) along z is used to reduce the local microscopic fluctuations.

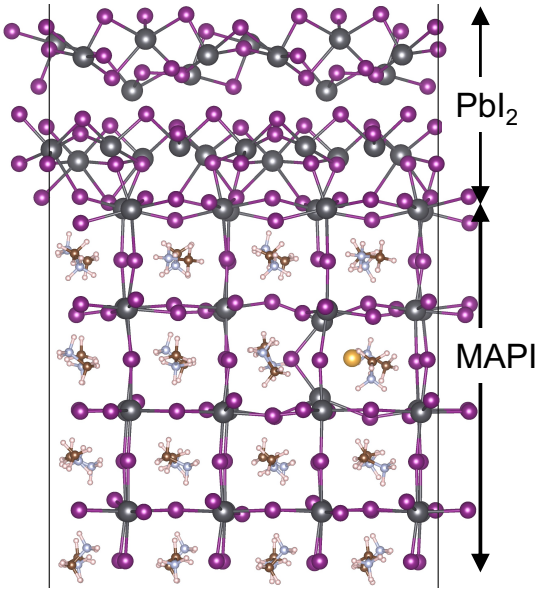

Figure S1: An I^-/V_I^+ Frenkel pair in MAPI located close to the interface with PbI_2. The interstitial I is shown in yellow and the vacancy is located in the layer above it. The interface is of the last type mentioned in the table i.e., MAPI (0 0 1) rotated 45 degrees about [0 0 1] axis with PbI_2 (1 0 $\bar{1}$ 0)

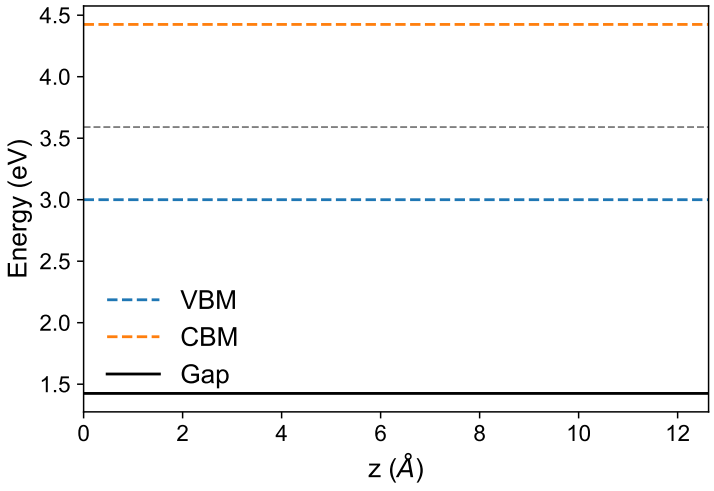

Figure S2: VBM and CBM energy levels of bulk MAPI obtained using the local density of states and $\Delta = 0.0002$.

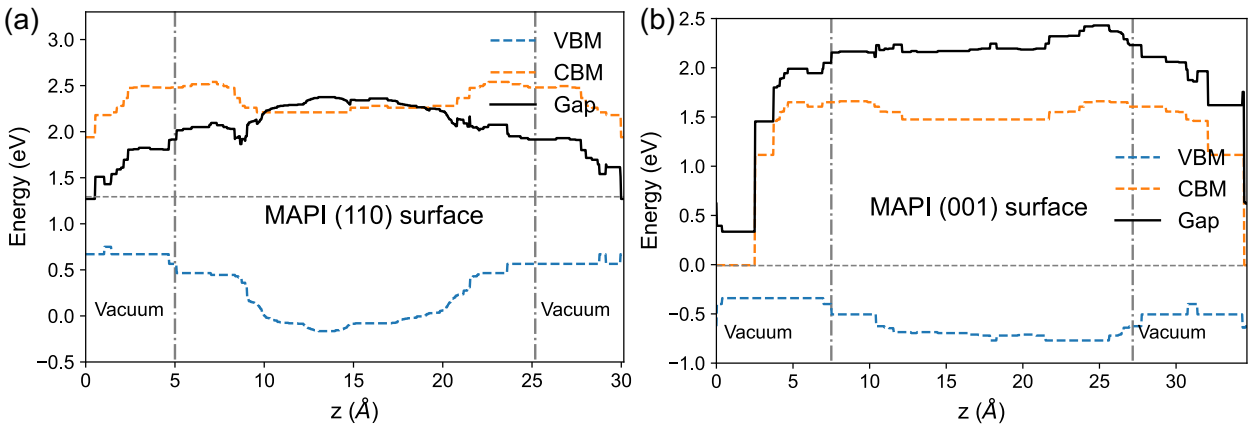

Figure S3: VBM and CBM energy levels as a function of the direction perpendicular to the surface/interface, z for (a) PbI_2 terminated MAPI (1 1 0) surface, (b) PbI_2 terminated MAPI (0 0 1) surface. Vertical gray lines indicate the approximate locations of the interfaces with vacuum while the horizontal gray lines denote the Fermi level E_F.

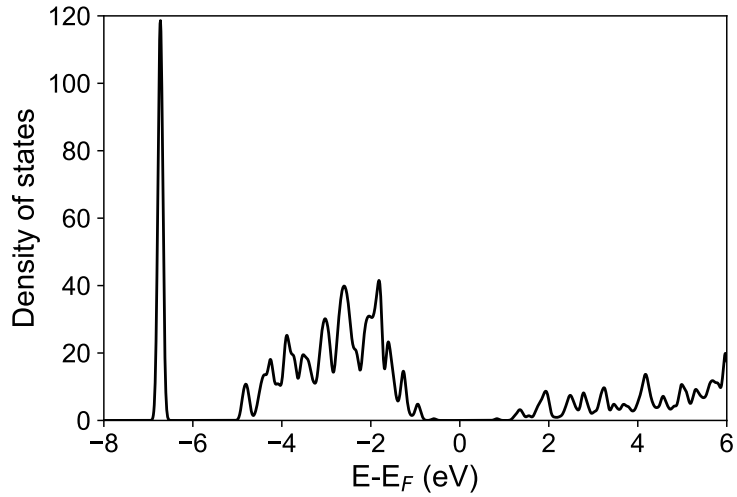

(a) Bulk MAPI. Gap: 1.42 eV

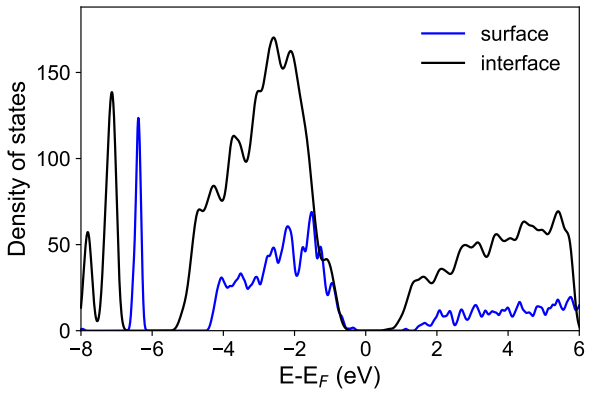

(b) MAPI slab and *Type 3* interface (Pb-terminated PbI_2). Slab Gap: 1.45 eV, Interface gap: 1.28 eV

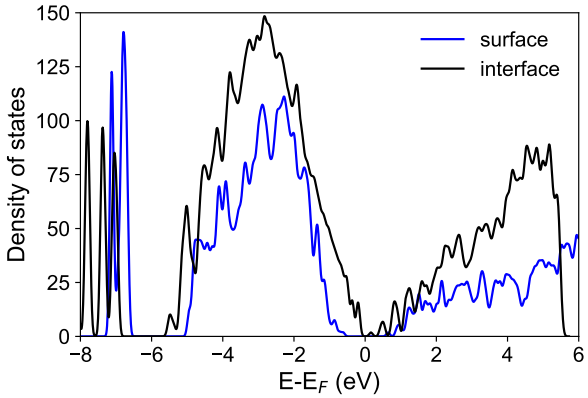

(c) MAPI slab and *Type 2* interface (Pb-terminated PbI_2). Slab gap: 1.26 eV, interface gap vanishing.

Figure S4: Comparison of electronic density of states between bulk, surfaces and interfaces of MAPI. The *type 3* interface maintains a gap close to the bulk while the *type 2* interface results in non-zero electronic density of states close to the Fermi level E_F.

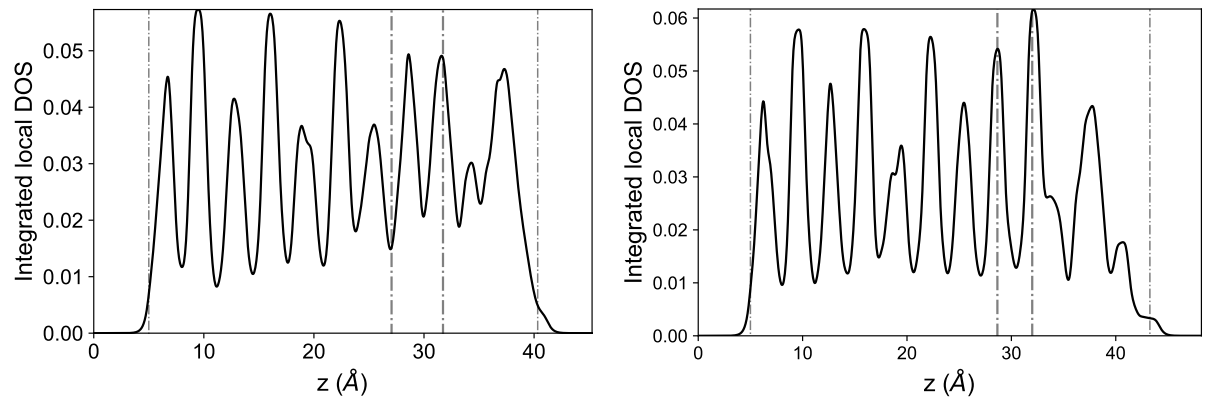

(a) *Type 2* interface (Pb-terminated PbI_2) (b) *Type 3* interface (Pb-terminated PbI_2)

Figure S5: Layer by layer integrated local electronic density of states i.e. $\int_{-\infty}^{E_F} D(E,z)dE$ for type 2 and type 3 interface. A macroscopic average of the local density of states is used for determining the band edges.

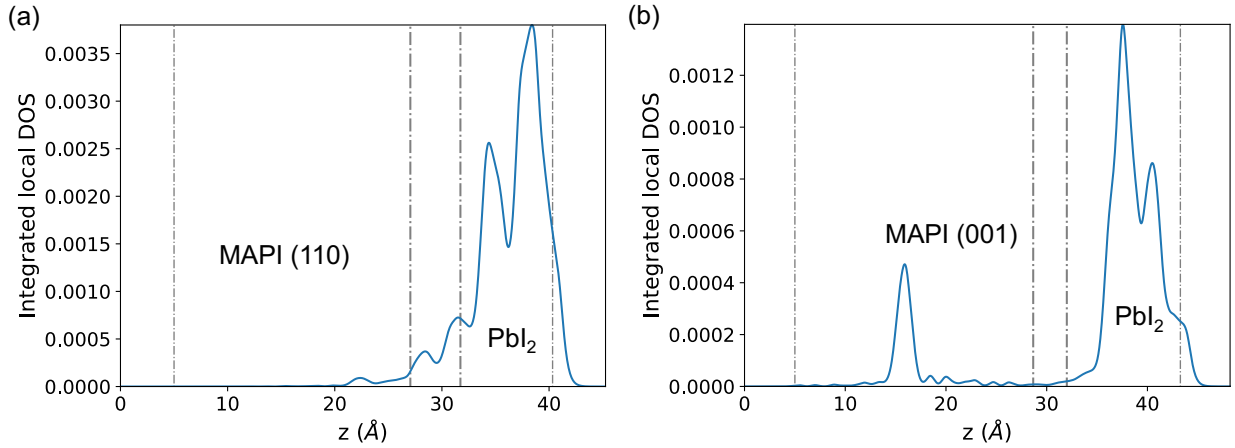

Figure S6: Integrated local density of states from 1 eV below the Fermi level to the Fermi level for (a) type 2 and (b) type 3 interfaces. The density is concentrated within PbI_2 layers.

Experimental Details

Sample preparation:

MAPI films were prepared according to previous reports.[19] 0.5 x 1 cm quartz substrates were prepared by sonicating in isopropyl alcohol followed by sonicating in acetone. The quartz slides were ozone cleaned for 15 minutes immediately before perovskite deposition. MAPI precursor solutions were made by dissolving MAI (Dyesol) and PbI_2 (Alfa Aesar, 99.9985%, metal basis, power) in a 9:1 N,N-dimethylformamide (DMF, Sigma Aldrich, anhydrous, 99.8%):dimethylsulfoxide (DMSO, Sigma Aldrich, anhydrous, >99.9%) solution. For the stoichiometric films (0% excess PbI2), 1.5 M films were made. To create films of other stoichiometric values, 2.5%, 5%, and 10% excess PbI_2 by molarity was added. These films were used for TR, TRPL, and XRD measurements.

Additional films for TRPL measurements were made with 0.75 and 0.375 M solutions. All solutions were prepared in a glovebox. Films were deposited using an antisolvent spin-coating method. 50 μL of the perovskite precursor solution was statically drop cast onto the films. The films were then spun at 4000 rpms for 25 seconds, with 60 uL of chlorobenzene (Sigma Aldrich, anhydrous, >99.8%) dynamically spun cast onto the film after 10 seconds of spin coating. The films were annealed for 1 minute at 65 C followed by 2 minutes at 100 C. Films were kept in a nitrogen flow box after deposition to ensure the films did not degrade under ambient conditions.

Transient reflectance measurements:

Transient reflectance measurements were performed on a Coherent Laser (800 nm fundamental beam, 1 kHz rep rate, 3 mJ/pulse, 100 fs pulse width) with a Helios Ultrafast spectrometer used for detection. The fundamental beam was split into the pump and probe pulse directly after the Coherent laser. The pump laser was tuned with a Palitra Duo OPA to obtain varying excitation wavelengths needed for TR measurements. The probe beam was sent through a delay line before being transformed into a white light continuum using a Sapphire crystal. The pump and probe pulses were aligned on the sample, with the probe

pulse at a 45° angle to the sample. All samples were measured under ambient conditions. The excitation density for each wavelength was kept so that N_0 was approximately 4 x 10^{17} charge carriers/cm^3.

Time resolved photoluminescence:

A Hamamatsu C10910-04 streak camera was used for detection and an NKT supercontinuum fiber laser (SuperK EXU-6-PP) for excitation. Samples were excited with 600 nm light.

Profilometry:

A Dektak 8 Advanced Development Profilometer was used to obtain sample thickness information. At least 3 scans were performed on each film and averaged to find the film thickness.

XRD:

X-ray diffraction patterns were measured with a Bruker D8 diffractometer equipped with a Hi-Star 2D area detector and a Cu Kαradiation source. Scherrer analysis was performed by fitting peaks to a Lorentzian profile.

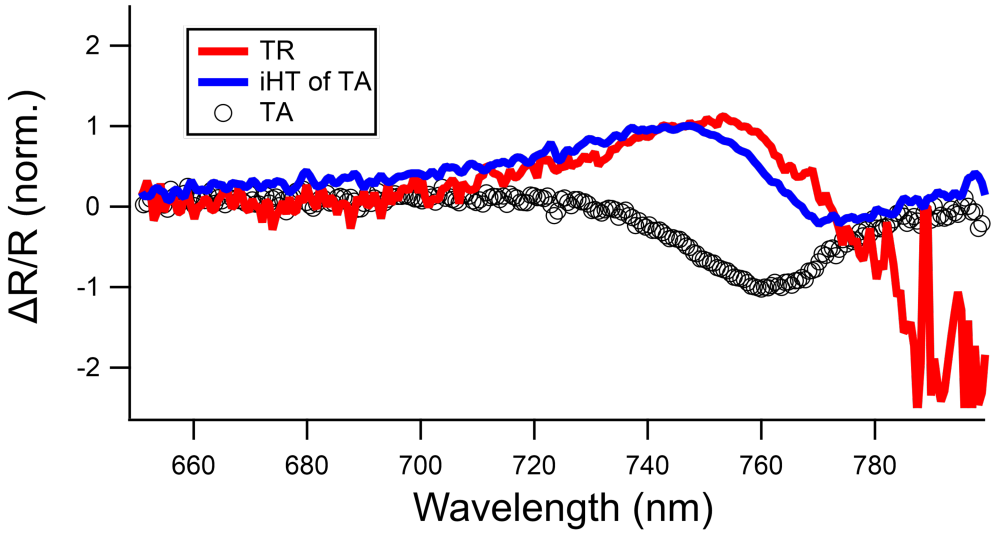

Figure S7: Transient absorption (grey circles), transient reflectance (red trace), and the inverse Hilbert transform of the transient absorption spectrum (blue trace). The TA signal shows a ground state bleach around 760 nm, typical of MAPI. Using the Kramers-Kronig relation, the transient absorption spectrum (grey) can be transformed into a simulation of the transient reflectance spectrum (blue). At wavelengths smaller than 750 nm (higher energy), the transform of the TA (blue) matches exactly with the transient reflectance spectrum (red). This indicates that at wavelength where the inverse Hilbert transform of the TA matches the TR, only changes in reflectance at the front (surface) of the sample is probed. Below 760 nm, an interference regime where signal from both the front and back surfaces of the perovskite is probed. This indicates that the kinetics for analysis should be taken from higher than 760 nm.

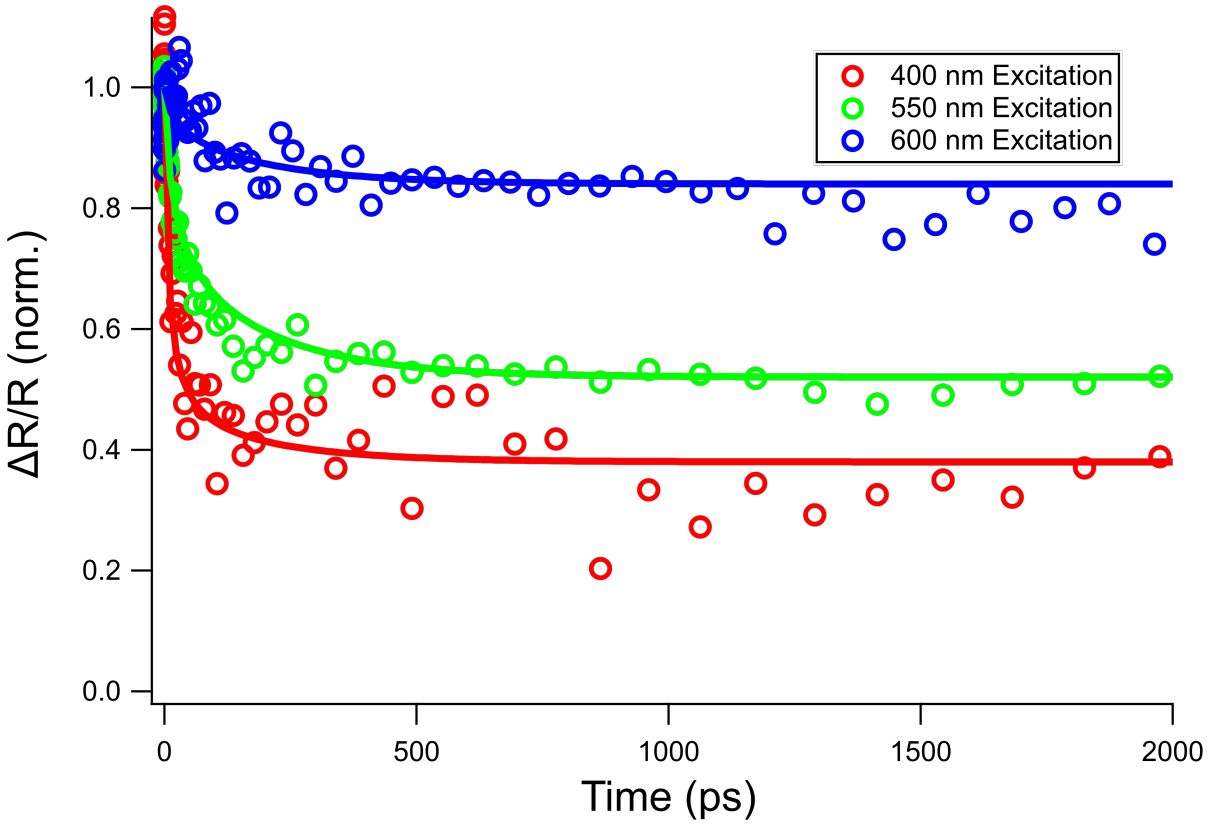

Figure S8: Transient reflectance kinetics (taken at 700 nm) for the 10% excess sample pumped at different wavelengths. Since the absorption coefficient of MAPI increases with increasing pump energies, lower energy pumps are able to excite farther into the film compared to high energy pumps. This allows for larger volumes of the film, and therefore more bulk-like (vs. surface) behavior, with decreasing pump energy. The higher the pump energy, the shorter the kinetic lifetime. Since the change in the signal across all three wavelengths is primarily concentrated to the first few hundred ps, then diffusion can be identified as the mechanism that contributes to the change in signal. Therefore, diffusion dominates at the surface. This data can be fit to a global analysis that can quantitatively extract the diffusion coefficient.[20] The fitting procedure was performed on raw data without normalization. The 10% excess sample is representative for the data for 0, 2.5, and 5% excess as well.

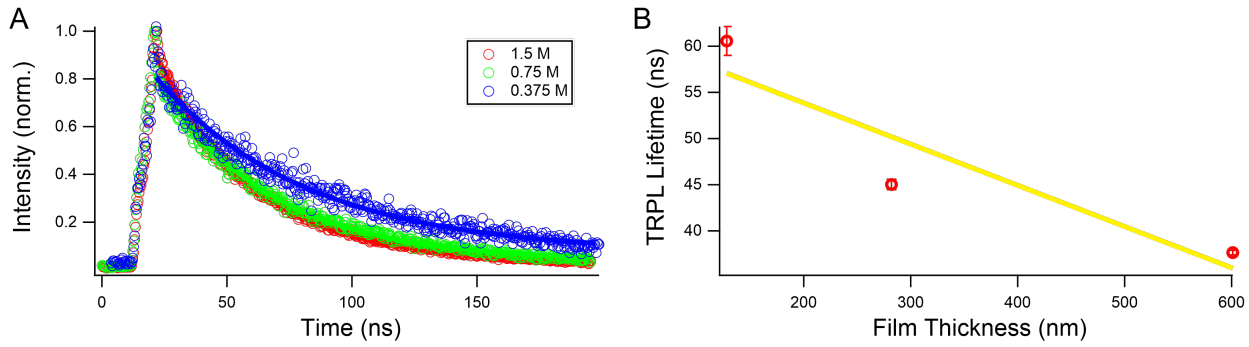

Figure S9: (A) Time resolved photoluminescence of 0% excess films. Films were made with precursors with varying molarity, which yields films with different thicknesses (as measured by profilometry, B). The films were excited with 600 nm light and the PL lifetime was then fit to a monoexponential decay. (B) The extracted lifetimes were then plotted against the film thickness so that a linear fit between TRPL lifetime and film thickness could be found. The inverse of this relationship yields the surface recombination lifetime in m/s. These results are reported in Fig. 4 of the main text.

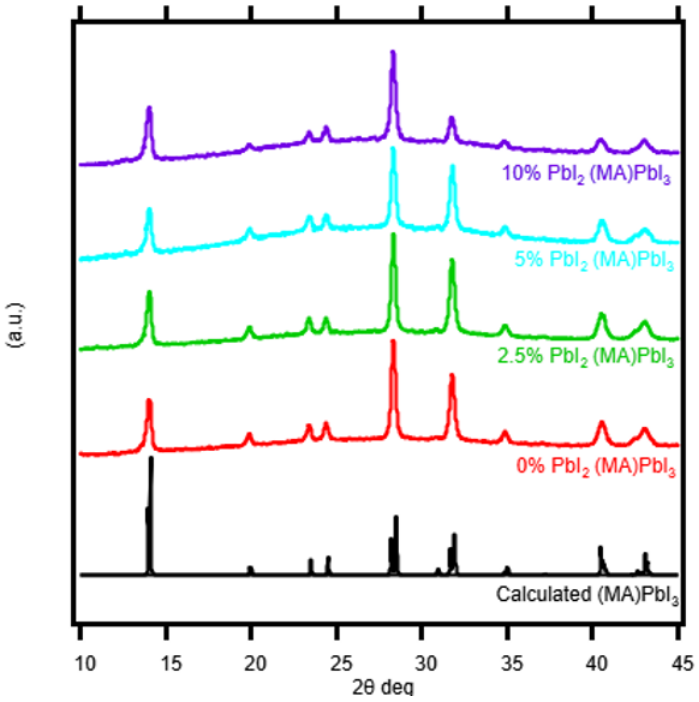

Figure S10: X-ray diffraction (XRD) patterns of freshly prepared MAPI thin films with varying PbI_2 content. The XRD patterns match well to the calculated MAPI pattern[21] and are absent of any impurity peaks. The average crystallite size calculated from the Scherrer equation is 56 nm, 56 nm, 51 nm, 52 nm for 0%, 2.5%, 5%, 10% PbI_2, respectively, indicating there is little variation with perovskite grain size with varying ratios of PbI_2 in the precursor.

References

(1) Giannozzi, P. et al. QUANTUM ESPRESSO: a modular and open-source software project for quantum simulations of materials. *J. Phys.: Condens. Matter* **2009**, *21*, 395502.

(2) Giannozzi, P. et al. Advanced capabilities for materials modelling with Quantum ESPRESSO. *J. Phys.: Condens. Matter* **2017**, *29*, 465901.

(3) Perdew, J. P.; Burke, K.; Ernzerhof, M. Generalized Gradient Approximation Made Simple. *Phys. Rev. Lett.* **1996**, *77*, 3865–3868.

(4) Heyd, J.; Scuseria, G. E.; Ernzerhof, M. Hybrid functionals based on a screened Coulomb potential. *J. Chem. Phys.* **2003**, *118*, 8207–8215.

(5) Grimme, S.; Antony, J.; Ehrlich, S.; Krieg, H. A consistent and accurate ab initio parametrization of density functional dispersion correction (DFT-D) for the 94 elements H-Pu. *J. Chem. Phys.* **2010**, *132*, 154104.

(6) Garrity, K. F.; Bennett, J. W.; Rabe, K. M.; Vanderbilt, D. Pseudopotentials for high-throughput DFT calculations. *Comput. Mater. Sci.* **2014**, *81*, 446–452.

(7) Schlipf, M.; Gygi, F. Optimization algorithm for the generation of ONCV pseudopotentials. *Comput. Phys. Commun.* **2015**, *196*, 36–44.

(8) Du, M.-H. Density Functional Calculations of Native Defects in CH3NH3PbI3: Effects of Spin–Orbit Coupling and Self-Interaction Error. *J. Phys. Chem. Lett.* **2015**, *6*, 1461–1466.

(9) Supasai, T.; Rujisamphan, N.; Ullrich, K.; Chemseddine, A.; Dittrich, T. Formation of a Passivating CH3NH3PbI3/PbI2 Interface during Moderate Heating of CH3NH3PbI3 Layers. *Appl. Phys. Lett.* **2013**, *103*, 183906.

(10) Ong, S. P.; Richards, W. D.; Jain, A.; Hautier, G.; Kocher, M.; Cholia, S.; Gunter, D.; Chevrier, V. L.; Persson, K. A.; Ceder, G. Python Materials Genomics (pymatgen): A robust, open-source python library for materials analysis. *Comput. Mater. Sci.* **2013**, *68*, 314 – 319.

(11) Larsen, A. H. et al. The atomic simulation environment—a Python library for working with atoms. *J. Phys.: Condens. Matter* **2017**, *29*, 273002.

(12) Momma, K.; Izumi, F. VESTA 3 for three-dimensional visualization of crystal, volumetric and morphology data. *J. Appl. Crystallogr.* **2011**, *44*, 1272–1276.

(13) Meggiolaro, D.; De Angelis, F. First-Principles Modeling of Defects in Lead Halide Perovskites: Best Practices and Open Issues. *ACS Energy Lett.* **2018**, *3*, 2206–2222.

(14) Stoumpos, C. C.; Malliakas, C. D.; Kanatzidis, M. G. Semiconducting Tin and Lead Iodide Perovskites with Organic Cations: Phase Transitions, High Mobilities, and Near-Infrared Photoluminescent Properties. *Inorg. Chem.* **2013**, *52*, 9019–9038.

(15) Wyckoff, R. W. G. Crystal structures, 2nd edition. *Acta Crystallogr.* **1963**, *1*, 239–444.

(16) Gražulis, S.; Chateigner, D.; Downs, R. T.; Yokochi, A. F. T.; Quirós, M.; Lutterotti, L.; Manakova, E.; Butkus, J.; Moeck, P.; Bail, A. L. Crystallography Open Database – an open-access collection of crystal structures. *J. Appl. Cryst.* **2009**, *42*, 726–729.

(17) Yamasaki, T.; Kaneta, C.; Uchiyama, T.; Uda, T.; Terakura, K. Geometric and Electronic Structures of $\mathrm{Si}{\mathrm{O}}_{2}/\mathrm{Si}(001)$ Interfaces. *Phys. Rev. B* **2001**, *63*, 115314.

(18) Anh Pham, T.; Li, T.; Nguyen, H.-V.; Shankar, S.; Gygi, F.; Galli, G. Band Offsets and Dielectric Properties of the Amorphous Si $_3$ N $_4$ /Si(100) Interface: A First-Principles Study. *Appl. Phys. Lett.* **2013**, *102*, 241603.

(19) Elmelund, T.; Scheidt, R. A.; Seger, B.; Kamat, P. V. Bidirectional Halide Ion Exchange in Paired Lead Halide Perovskite Films with Thermal Activation. *ACS Energy Lett.* **2019**, *4*, 1961–1969.

(20) Zhai, Y.; Wang, K.; Zhang, F.; Xiao, C.; Rose, A. H.; Zhu, K.; Beard, M. C. Individual Electron and Hole Mobilities in Lead-Halide Perovskites Revealed by Noncontact Methods. *ACS Energy Lett.* **2020**, *5*, 47–55.

(21) Szafrański, M.; Katrusiak, A. Mechanism of Pressure-Induced Phase Transitions, Amorphization, and Absorption-Edge Shift in Photovoltaic Methylammonium Lead Iodide. *J. Phys. Chem. Lett.* **2016**, *7*, 3458–3466, PMID: 27538989.